Tuning Double Layer Structure of WO_3 Nanobelt for Promoting the Electrochemical Nitrogen Reduction Reaction in Water①

HONG Qing-Shui② LI Tang-Yi② ZHENG Shi-Sheng
CHEN Hai-Biao CHU Hong-Hao XU Kuan-Da
LI Shun-Ning MEI Zong-Wei ZHAO Qing-He
REN Wen-Ju ZHAO Wen-Guang PAN Feng③
(*School of Advanced Materials, Peking University, Shenzhen Graduate School, Shenzhen, Guangdong* 518055, *China*)

ABSTRACT Electrochemical fixation of nitrogen to ammonia with highly active, highly selective and low cost electrocatalysts is a sustainable alternative to the extremely energy- and capital-intensive Haber-Bosch process. Herein, we demonstrate a near electroneutral WO_3 nanobelt catalyst to be a promising electrocatalyst for selective and efficient nitrogen reduction. The concept of near electroneutral interface is demonstrated by fabricating WO_3 nanobelts with small zeta potential value on carbon fiber paper, which ensures a loose double layer structure of the electrode/electrolyte interface and allows nitrogen molecules access the active sites more easily and regulates proton transfer to increase the catalytic selectivity. The WO_3/CFP electrode with optimal surface charge achieves a NH_3 yield rate of 4.3 $\mu g \cdot h^{-1} \cdot mg^{-1}$ and a faradaic efficiency of 37.3% at −0.3 V *vs.* RHE, rivalling the performance of the state-of-the-art nitrogen reduction reaction electrocatalysts. The result reveals that an unobstructed gas-diffusion pathway for continually supplying enough nitrogen to the active catalytic sites is of great importance to the overall catalytic performance.

Keywords: electrochemical nitrogen reduction reaction, zeta potential, nitrogen diffusion and transport process, WO_3 nanobelts, first-principles calculations; DOI: 10.14102/j.cnki.0254–5861.2011–2975

1 INTRODUCTION

Activating dinitrogen (N_2) in the atmosphere to produce ammonia (NH_3) has stimulated intensive researches on associated mass production technology due to the great importance of NH_3 in sustaining lives on earth[1, 2]. The conventional Haber-Bosch process for NH_3 production dissociates the strong N≡N triple bonds (dissociative mechanism) under harsh reaction conditions, and thus suffers from high energy consumption and carbon dioxide emission[3]. On the basis of proton-coupled electron transfer (PCET) reaction, sequential hydrogenation of N_2 molecules (associative mechanism) under mild conditions is an alternative to dissociating N≡N bonds directly in the nitrogen reduction reaction[4]. With utilizing renewable electricity, the electrochemical nitrogen reduction reaction (ENRR) offers a potentially sustainable approach to produce NH_3 without demanding requirements on pressure, heat and energy[5, 6]. However, the development of this process remains experimental due to the lack of efficient electrocatalysts possessing the ability to adsorb and reduce N_2 to NH_3 with sufficient activity and selectivity. Despite tremendous efforts in recent decades, most electrocatalysts show a higher overpotential for the ENRR than the hydrogen evolution reaction (HER) in aqueous solutions, which results in a low NH_3 yield rate (r_{NH3}) and a poor faradaic efficiency (FE). Additionally, the mechanism of ENRR is complicated and has not been completely elucidated[7, 8].

More recently, studies for promoting the ENRR using noble-metal/transition-metal-based catalysts and novel

Received 2 September 2020; accepted 28 October 2020

① This work was supported by Shenzhen Science and Technology Research Grant (ZDSYS201707281026184) and Natural Science Foundation of Shenzhen (JCYJ20190813110605381)

② Author contributions. Q.S.H and T.Y.L contributed equally

③ Corresponding author. E-mail: panfeng@pkusz.edu.cn

electrolyte additives have been reported[9-14]. ENRR using hollow gold nanocages as effective electrocatalysts can achieve a maximum r_{NH3} of 3.4 $\mu g \cdot h^{-1} \cdot cm^{-2}$ at −0.5 V *vs.* RHE and a FE of 30.2% at −0.4 V *vs.* RHE, respectively[15]. Tungsten oxide with tailored surface oxygen vacancies has been reported as efficient catalyst for N_2 fixation to realize efficient binding and reduction of N_2 at low overpotentials, showing an r_{NH3} of 4.2 $\mu g \cdot h^{-1} \cdot mg^{-1}$ but a low FE of 6.8% at −0.12 V *vs.* RHE[16]. In addition to catalysts, Rondinone *et al.* reported that the counterions (Li^+, Na^+, K^+) in the electrolyte were also vital to ENRR and suggested the smallest counterions could increase the N_2 concentration to an extreme within the Stern layer, resulting in an improved FE (from 2.75% to 11.56% on carbon nanospike catalyst)[17]. Although progress has been made in sustainable electrochemical N_2 fixation, simultaneous promotion of selectivity and activity in state-of-the-art catalytic systems remains to be a challenge. Moreover, the double layer structure of catalyst/electrolyte interface receives very limited attention, which is actually of great importance because a desirable catalyst/electrolyte interface should favor the mass transfer from the electrolyte to the catalyst surface.

Theoretical calculations showed that modulating the reaction thermodynamics of the generation of ENRR intermediates and HER at the surface could both greatly suppress HER and make the surface proton transfer to ENRR process preferentially in transition-metal oxide catalytic system[18, 19]. Here, we report that WO_3 nanobelts with (001) facet exposed act as an efficient electrocatalyst for ENRR under ambient conditions. Surface oxygen vacancies (OVs) on WO_3 nanobelts can offer a lower ΔG of the initial reaction step for ENRR than HER and thus obtain high intrinsic ENRR activity and selectivity. The electroneutral surface of WO_3 is actually of great importance, which renders a nitrogen-friendly surface property to allow the access of reactive catalytic sites by the N_2 molecule readily. The WO_3 nanobelts with near electroneutral surface can promote the ENRR to achieve a record-high FE of 37.3% in aqueous solutions.

2 RESULTS AND DISCUSSION

We directly fabricated the tungsten oxide on carbon fiber paper (CFP) current collector by a one-step *in-situ* hydrothermal synthesis, as illustrated in Fig. 1. Fig. 2a shows that the pristine CFP consists of well-connected carbon fibres with a diameter of ~10 μm and it is a three-dimensional conductive network for supporting catalysts. After hydrothermal synthesis, the carbon fibres are densely wrapped in a large number of WO_3 aggregates (Fig. 2b), most of which are belt-like with large exposed flat surfaces, as demonstrated in Fig. 2c. Low- and high-magnification TEM (HRTEM) images in Figs. S1b and S1c reveal that the WO_3 aggregates are piled up from arrays of several individual narrow belts of 5～10 nm wide attached side by side. Without the need for further treatments, the WO_3 layer synthesized on the surfaces of CFP showed excellent adhesion and survived repeated washing with deionized water.

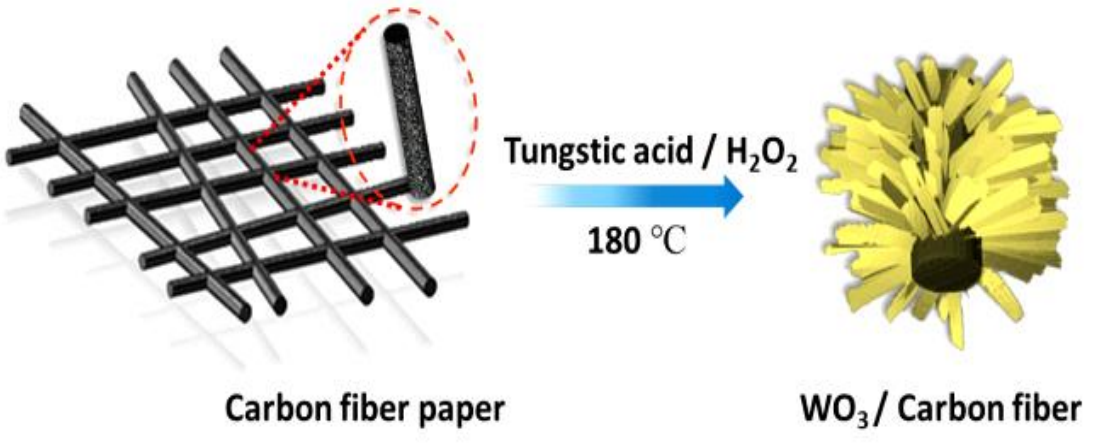

Fig. 1. Schematic illustration of one-step synthetic route for WO_3/CFP by a non-template, self-assembled hydrothermal reaction of tungstic acid, which was used directly as a high performance ENRR catalytic electrode

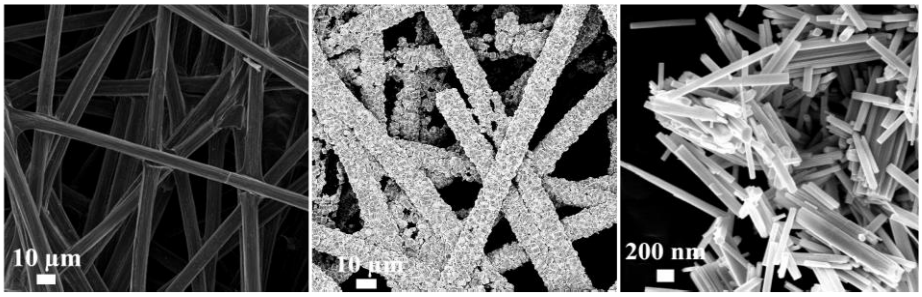

(a) (b) (c)

Fig. 2. SEM of (a) bare CFP, (b) WO_3 nanobelts/CFP and (c) the enlarged image of WO_3 nanobelts

XRD result in Fig. 3a and selected area electron diffraction (SAED) pattern in Fig. S1d confirm that the as-prepared WO_3 crystallized to the hexagonal structure (space group *P*6/*mmm* (191)) as polycrystals. HRTEM image in Fig. 3b displays that an individual WO_3 nanobelt has a lattice plane spacing of 0.365 nm, which corresponds to the (110) plane spacing of hexagonal WO_3 phase. Accordingly, the exposed surface of a typical WO_3 nanobelt is inferred as the (001) facet. During the hydrothermal treatment, likely the (001) faces of the WO_3 preferentially adsorb SO_4^{2-} ions, forming a strong energy barrier to direct two-dimensional crystal growth perpendicular to the [001] direction[20]. Many missing points and amorphous regions can be observed, as labelled in Fig. 3b. These discontinuous regions are probably the locations of oxygen vacancies[21]. The chemical state of the as-synthesized WO_3 was further characterized by XPS. As shown in Fig. 4a, pronounced doublet peaks at 35.3 and 37.4 eV are observed, and they belong to $4f_{7/2}$ and $4f_{5/2}$ of W^{6+} due to the spin-orbital splitting. Weak doublet peaks centred at 34.7 and 36.3 eV are assigned to the typical binding energies of W^{5+} $4f_{7/2}$ and W^{5+} $4f_{5/2}$ with spin-orbit splitting, respectively. The observation of W^{5+} signals could be related to the presence of OVs[22]. In addition, the O 1*s* XPS spectrum in Fig. 4b also shows that besides the major peak at 529.9 eV corresponding to the binding energy of lattice oxygen, a fitting peak at 531.4 eV can be differentiated, which could be attributed to the adsorbed oxygen species at the defect sites where lattice oxygen is missing[23].

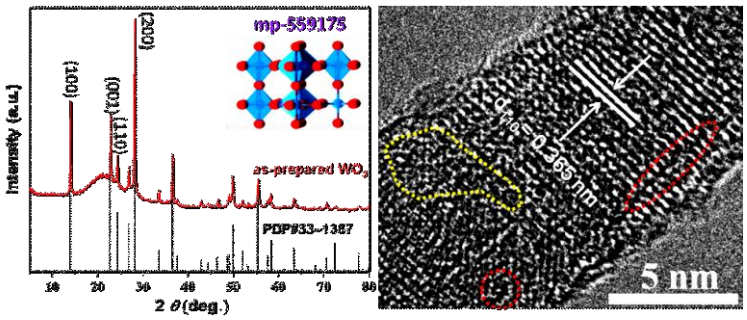

(a) (b)

Fig. 3. (a) XRD pattern and (b) HRTEM of the synthesized WO_3

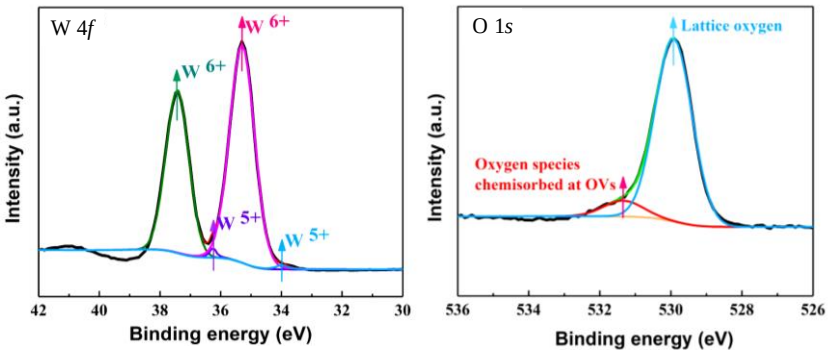

(a) (b)

Fig. 4. High-resolution XPS of (a) W 4*f* and (b) O 1*s* for the WO_3

The ENRR activities of this WO_3 nanobelt material with (001) facet exposed and surface oxygen defects loaded on CFP were first studied in aqueous electrolyte containing potassium cations (0.5 M K_2SO_4) and compared with corresponding reference materials. Fig. 5 presents the key electrochemical results and demonstrates that the WO_3/CFP could guarantee both high ENRR catalytic activity and suppressed HER. As shown in Fig. 5a, in contrast to the overlapping CVs in Ar- and N_2-saturated solution for CFP and WO_{3-x}/CFP, the difference between the two sets of CV data for WO_3/CFP is striking: in N_2-saturated solution, no obvious well-defined oxidative peaks for reversible hydrogen oxidation can be observed. Nevertheless, a remarkable oxidative peak appears at approximately 1.5 V, which is possibly associated with oxygen evolution by water oxidation as referred to the testing result in Ar-saturated solution. As another direct evidence of nitrogen fixation products formation on WO_3 surface, the newly-presented chemisorbed ammonium can be detected on the surface of the catalyst by XPS (Fig. S6b). The ENRR experiments were then conducted under various potentials ranging from −0.15 to −0.6 V for 2 h (as shown in Fig. 5b). It is worth mentioning that no ammonia can be detected in Ar-saturated solution at −0.3 V or electrolytes bubbled by nitrogen at open circuit potential after 12 h test for all samples (Fig. S3), which could exclude the contamination from the catalyst and environment to the amount of ammonia produced. Bare CFP showed no activity due to the lack of active sites for catalysing ENRR. Fig. 6a presents the calculated results of r_{NH3} and FE for WO_3/CFP at different potentials in N_2-saturated solution. Obviously, the rate of NH_3 formation steadily increases and reaches 7.6 $\mu g \cdot h^{-1} \cdot cm^{-2}$ at −0.6 V, whereas the FE first increases and then declines sharply from 37.3% to 1.94% as the potential becomes more negative, which probably results from the competitive HER at a high overpotential. Interestingly, the ratio of NH_3 production progressively enhances as the overpotential reduces, indicating that the $*N_2$ adsorbates on WO_3 are hydrogenated preferentially during electrolysis. These values of r_{NH3} and FE for WO_3/CFP are among the best to our knowledge, as compared to the recently reported electrocatalysts (Table S2).

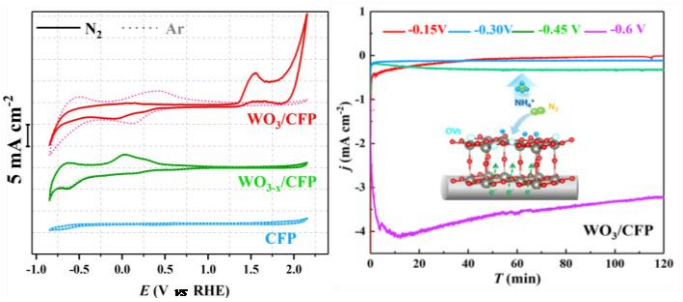

(a) **(b)**

Fig. 5. (a) CVs of CFP, WO_{3-x}/CFP and WO_3/CFP in Ar- (dotted line) and N_2-saturated (solid lines) 0.5 M K_2SO_4 at 50 $mV \cdot s^{-1}$. (b) Chrono-amperometry measurements at various potentials over WO_3/CFP

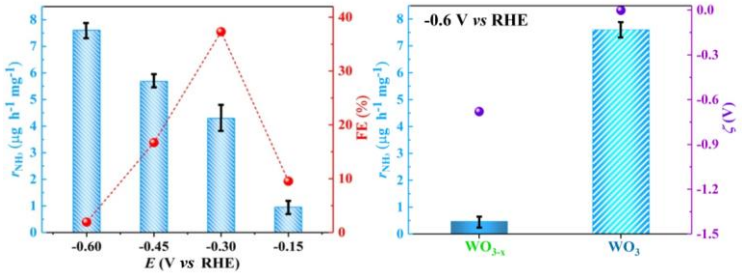

(a) **(b)**

Fig. 6. (a) Mean ammonia yields (r_{NH3}, left axis) and Faradaic efficiencies (FE, right axis) for WO_3/CFP at different electrode potentials. Error bars in the histograms indicate the standard deviation for three times measurements. (b) Ammonia yields (r_{NH3}, left axis) for WO_3/CFP and WO_{3-x}/CFP at -0.6 V *vs.* RHE and the zeta potential (ζ, right axis) of their corresponding catalysts

Theoretically, r_{NH3} can be further improved by introducing more oxygen vacancies to the surface to enhance the surface adsorption and activation of nitrogen. Therefore, control experiments using ethanol-treated reference samples are also conducted under the same conditions. Fig. 7a compares the XRD patterns of WO_3 and its comparative samples WO_{3-x}.

The lattice integrity of WO_{3-x} was maintained after ethanol processing for 0.5 h. The chemical status of WO_{3-x} with crystalline structure largely preserved was characterized by XPS. Results of WO_{3-x} in Fig. 7b and c reveal that the integrated peak intensities of the W^{5+} and adsorbed oxygen species both increase in comparison to that of WO_3, which implies that ethanol treatment can promote the formation of OVs through surface reduction. As another piece of evidence, the major peaks of W 4*f* binding energy for WO_{3-x} display a slight shift towards higher binding energy in comparison to that of WO_3, which is likely ascribed to the increase of oxygen vacancies. The existence and concentration of OVs were further verified by electron spin resonance (ESR) spectroscopy. As shown in Fig. S2, WO_{3-x} rather than WO_3 exhibits a significant ESR signal at g = 2.002, suggesting the electron trapping at OVs. The concentration of OVs in the samples follows the order WO_{3-x} > WO_3. Unexpectedly, as shown in Fig. 6b, the WO_{3-x}/CFP with higher concentration of OVs offers much smaller r_{NH3} of 0.48 $\mu g \cdot h^{-1} \cdot cm^{-2}$ at –0.6 V. To understand this abnormal phenomenon, we carried out EDS analysis on these electrodes after electrolysis. As shown in Fig. 8a and b, scarcely any (W:K = 95:5, atomic ratio) or very small amount (W:K = 87:13, atomic ratio) of potassium cations can be detected on the surface of WO_3 with the removal of N_2- and Ar-saturated solvent. In contrast, tremendous amounts (W:K = 53:47, atomic ratio) of potassium cations were found on the surface of WO_{3-x} (as shown in Fig. 8c). This difference in surface-adsorbed potassium cations should be related to the double layer structure of their corresponding characteristic catalyst/electrolyte interface. Therefore, to understand the correlation between the double layer structure and the ENRR activity, we further examined the ζ-potentials of catalysts suspended in Ar- and N_2-saturated 0.5 M K_2SO_4 aqueous solution. A lower absolute value of ζ-potential suggests a looser double layer structure at the catalyst/electrolyte interface. As shown in Table S1, WO_3 exhibits a ζ-potential of –33 mV in Ar-saturated solution, much lower than that of WO_{3-x} (–470 mV). Noticeably, an obvious reduction to nearly zero (–1.2 mV) in the absolute value of ζ-potential can be further observed in N_2-saturated electrolyte for WO_3 sample, which might be caused by the effect of chemisorbed N_2 toward active sites that change the charge characteristics of catalyst surface. These ζ-potential results are in good agreement with the observation of EDS images, indicating entirely different double layer structure of catalyst/electrolyte interface for WO_3 and WO_{3-x} during ENRR. According to the above results, when the catalyst/electrolyte interface does not form a strong electrical double layer (EDL), N_2 molecules will be more energetically favorable to diffuse and transfer to the catalyst surface, which is actually of great importance because the effective N_2 adsorption is the first reaction step in ENRR, and ultimately decides the occurrence of ENRR. In order to further verify the influence of EDL on ENRR, we tested the as-made electrodes in four electrolytes containing different alkali-metal cations (Li^+, Na^+, K^+ and Cs^+). The results of regulating effect of alkali metal cations are shown in Fig. S4. As another strong piece of evidence, there are no obvious variations of NH_3 production for the WO_3/CFP in the four electrolytes (Fig. S4a). However, the variation tendency of NH_3 production for WO_{3-x}/CFP follows the same sequence: Li^+ > Na^+ > K^+ > Cs^+ (Figs. S4b and S4c). This difference could be primarily as a result of the catalyst/electrolyte interface structures. Since small alkali metal cations are suggested to reduce the EDL thickness, leaving the catalyst surface is more available for N_2 diffusion and adsorption[4]. Because the WO_{3-x}/CFP has a strong EDL on its own catalyst surfaces, the ENRR activities will be much more dependent on alkali metal cations in the electrolyte than WO_3/CFP. These results are consistent with the previous results in Fig. 6b and strongly imply a correlation between the efficiency of NH_3 production and catalyst/electrolyte interface structure.

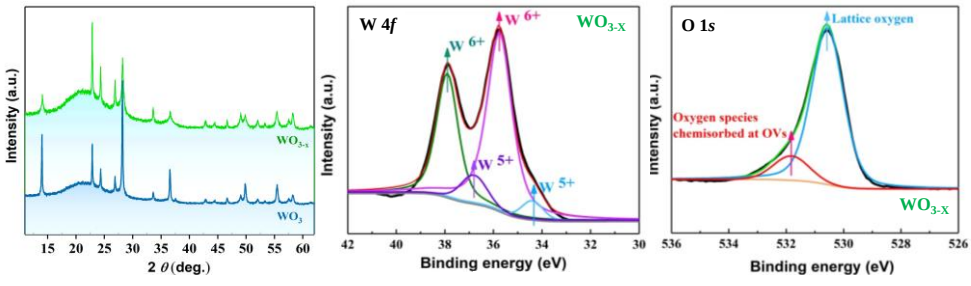

(a) **(b)** **(c)**

Fig. 7. (a) Comparison XRD patterns of WO_3 and WO_{3-x}. (b) W 4*f* and (c) O 1*s* XPS spectra of WO_{3-x}

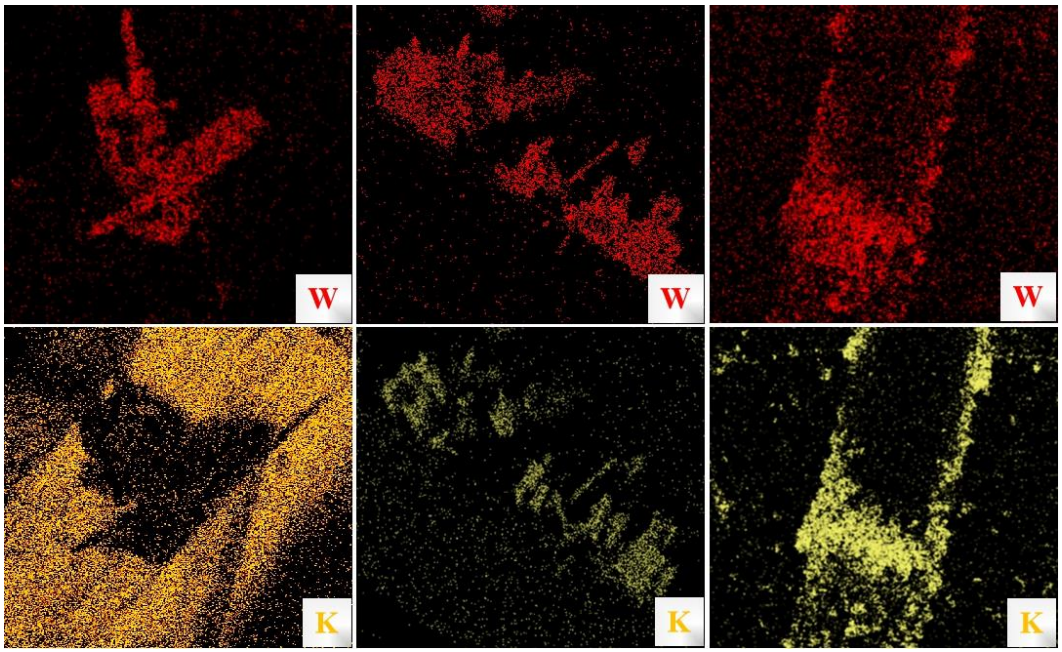

(a) WO_3/CFP, N_2 **(b) WO_3/CFP, Ar** **(c) WO_{3-x}/CFP, N_2**

Fig. 8. Elemental mapping revealing the elemental distribution of W and K on the surface of electrodes after electrolysis. WO_3/CFP in (a) N_2- and (b) Ar-saturated 0.5 M K_2SO_4. (c) WO_{3-x}/CFP in N_2-saturated 0.5 M K_2SO_4

Lastly, we performed DFT calculations for the energetics of HER and ENRR steps at the OVs on the most stable (001) facet of WO_3 to investigate catalytic selectivity and activity for ENRR process on WO_3 with OVs[16]. All possible reaction intermediates of ENRR have been taken into account to obtain the free energy diagram and the corresponding potential determining step (PDS) along the reaction pathway (Computational details are provided in the Supporting Information). PDS represents the elementary step with the largest positive free energy change and determines the overpotential of the ENRR process[24]. As shown in Fig. 9, six hydrogenation steps are involved in the formation of NH_3 (configurations shown in Fig. S5), and the final step ($*NH_2 \rightarrow *NH_3$) turns out to be PDS. At the initial reaction step in ENRR, the free energy change of N_2 adsorption (ΔG_{*N2}) on OVs-WO_3 (001) is exothermic (−1.29 eV), while the $\Delta G_{*H}{}^{+}$ on OVs-WO_3 (001) is −0.53 eV, indicating the high selectivity of OVs-WO_3 (001) towards N_2 adsorption. Therefore, OVs can regulate the proton diffusion process to make the reaction more selective to ENRR in a vacuum condition. Furthermore, the $*N_2$ species bound strongly to W surfaces can be revealed by the projected density of states (pDOS) of $*N_2$. The W 5*d* band and the N_{ads} (the N atom directly bound to the surface) 2*p* orbitals overlap both below and above the Fermi level (Fig. S6a). The stronger interactions between $*N_2$ and the catalyst surfaces could stabilize the adsorbates, reduce the energy barriers of the subsequent hydrogenation steps and thus enhance the ENRR activity. According to the above results, we propose a feasible mechanism for promoting ENRR on WO_3 from the perspective of N_2 diffusion and transport in catalyst/electrolyte interface, as shown in Fig. 10a and b. With a very small ζ-potential, WO_3/electrolyte interface does not form a strong EDL. The charged species (hydrated SO_4^{2-} and K^+ ions) and neutral molecules (hydrated N_2) are randomly and loosely scattered on the vicinity of the WO_3 surface. Due to its lower adsorption barrier than proton, N_2 molecules will be more energetically favorable to diffuse and transfer to the OVs active sites. In contrast, a high absolute value of ζ-potential of WO_{3-x} surface implies the formation of a strong EDL on WO_{3-x}/electrolyte interface. The nitrogen-diffusion process is blocked and thereby the interface cannot create enough reaction contact point for ENRR. In addition to the first step in ENRR, OVs can further activate N_2 and lead to consecutive hydrogenation steps rather than HER. Therefore, it is likely that the unrestricted N_2 adsorption and low overpotential of ENRR on OVs-WO_3 are responsible for the significantly improved performance.

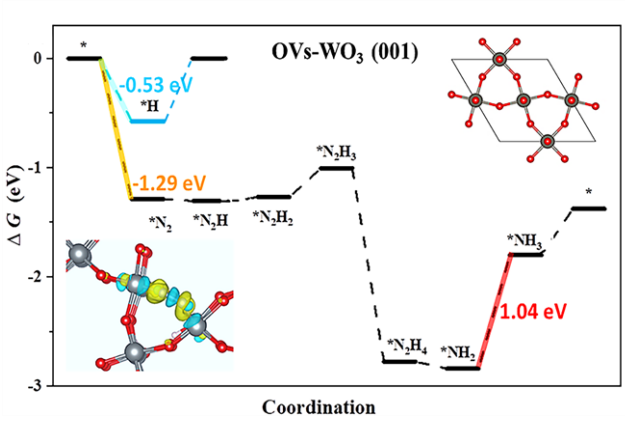

Fig. 9. Theory predicts the high selectivity of OVs on WO_3 (001) facet towards HER and ENRR in vacuum. The cyan and black lines indicate free energy diagram of adsorption energies of H^+ and ENRR on OV-WO_3 (001), respectively. Upper right shows the top view of WO_3 (001) surface. Bottom left shows the view of charge density difference of the N_2-adsorbed on WO_3 (001) surface. The yellow and blue isosurfaces represent charge accumulation and depletion in the space, respectively. After nitrogen adsorption, the electron depletes on the OV and accumulates on the adsorbed N_2, suggesting the possible N−N triple bond activation

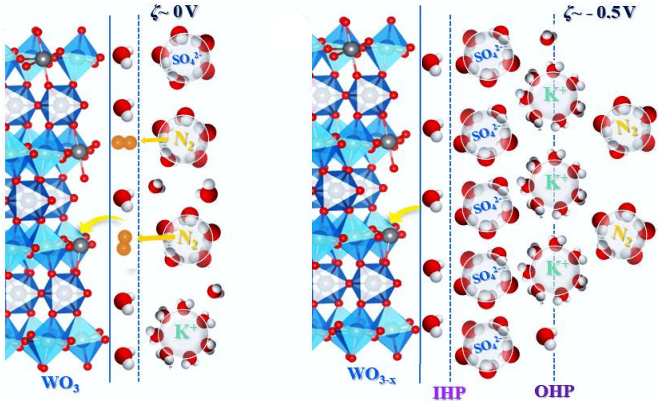

(a) ENRR favored **(b) HER favored**

Fig. 10. (a) Schematic illustration of the WO_3 with optimal surface charge structure for highly facilitating the N_2 diffusion and transport kinetics on catalyst/electrolyte interface in N_2-saturated K_2SO_4 media. (b) Structure of WO_{3-x} (large zeta potential)/electrolyte interface in N_2-saturated K_2SO_4 media. IHP is the inner Helmholtz plane, and OHP is the outer Helmholtz plane. Water molecules orient themselves toward the catalysts and form the solvation layer within the IHP. Beyond the outer OHP, the charged species and neutral molecules are loosely scattered in the electrolyte

3 CONCLUSION

In summary, we have developed a facile and effective synthesis approach to prepare surface charge optimized WO_3 nanobelts via a one-pot hydrothermal method. Surface OVs in WO_3 nanobelts exhibits more negative ΔG (*N_2) than ΔG (*H^+), suggesting a potential suppression of HER and dramatic improvements in the ENRR/HER selectivity. Our strategy also shows how to improve NH_3 production by regulating the N_2 molecule transfer process within the catalyst/electrolyte interface. WO_3 nanobelts with electro-neutral surfaces are successfully proven as a highly active and selective electrocatalyst for ENRR under ambient conditions with a NH_3 yield of 4.3 $\mu g \cdot h^{-1} \cdot mg^{-1}$ and a FE of 37.3% at −0.3 V *vs.* RHE, outperforming WO_{3-x} with larger zeta potential in an aqueous electrolyte. Following this strategy, future studies may find electrocatalytic systems with even higher ENRR performance in water by rational design of surface defects and modulating the EDL structure on the catalyst/electrolyte interface.

REFERENCES

(1) Jiao, D.; Iniguez, J. A.; Chong, L. Electrocatalytic nitrogen reduction at low temperature. *Joule* **2018**, 2, 846−56.

(2) Cui, X.; Tang, C.; Zhang, Q. A review of electrocatalytic reduction of dinitrogen to ammonia under ambient conditions. *Adv. Energy Mater*. **2018**, 8. 1800369−25.

(3) van der Ham, C. J. M.; Koper, M. T. M.; Hetterscheid, D. G. H. Challenges in reduction of dinitrogen by proton and electron transfer. *Chem. Soc.*

Rev. **2014**, 43, 5183–5191.

(4) Cao, N.; Zheng, G. Aqueous electrocatalytic N_2 reduction under ambient conditions. *Nano Res.* **2018**, 11, 2992–3008.

(5) Suryanto, B. H. R.; Kang, C. S. M.; Wang, D.; Xiao, C.; Zhou, F.; Azofra, L. M.; Cavallo, L.; Zhang, X.; MacFarlane, D. R. Rational electrode-electrolyte design for efficient ammonia electrosynthesis under ambient conditions. *ACS Energy Lett.* **2018**, 3, 1219–1224.

(6) Bao, D.; Zhang, Q.; Meng, F. L.; Zhong, H. X.; Shi, M. M.; Zhang, Y.; Yan, J. M.; Jiang, Q.; Zhang, X. B. Electrochemical reduction of N_2 under ambient conditions for artificial N_2 fixation and renewable energy storage using N_2/NH_3 cycle. *Adv. Mater.* **2017**, 29, 1604799–5.

(7) He, D.; Li, Y.; Ookap, H.; Go, Y. K.; Jin, F.; Kim, S. H.; Nakamura, R. Selective electrocatalytic reduction of nitrite to dinitrogen based on decoupled proton-electron transfer. *J. Am. Chem. Soc.* **2018**, 140, 2012–2015.

(8) Chen, G. F.; Cao, X.; Wu, S.; Zeng, X.; Ding, L. X.; Zhu, M.; Wang, H. Ammonia electrosynthesis with high selectivity under ambient conditions via a Li^+ incorporation strategy. *J. Am. Chem. Soc.* **2017**, 139, 9771–9774.

(9) Shi, M. M.; Bao, D.; Li, S. J.; Wulan, B. R.; Yan, J. M.; Jiang, Q. Anchoring PdCu amorphous nanocluster on graphene for electrochemical reduction of N_2 to NH_3 under ambient conditions in aqueous solution. *Adv. Energy Mater.* **2018**, 8, 1800124–6.

(10) Wang, Z.; Gong, F.; Zhang, L.; Wang, R.; Ji, L.; Liu, Q.; Luo, Y.; Guo, H.; Li, Y.; Gao, P.; Shi, X.; Li, B.; Tang, B.; Sun, X. Electrocatalytic hydrogenation of N_2 to NH_3 by MnO: experimental and theoretical investigations. *Adv. Sci.* **2019**, 6, 1801182–8.

(11) Du, H.; Guo, X.; Kong, R. M.; Qu, F. Cr_2O_3 nanofiber: a high-performance electrocatalyst toward artificial N fixation to NH_3 under ambient conditions. *Chem. Commun.* **2018**, 54, 12848–12851.

(12) Zhang, R.; Ji, L.; Kong, W.; Wang, H.; Zhao, R.; Chen, H.; Li, T.; Li, B.; Luo, Y.; Sun, X. Electrocatalytic N_2-to-NH_3 conversion with high faradaic efficiency enabled using a Bi nanosheet array. *Chem. Commun.* **2019**, 55, 5263–5266.

(13) Cui, X.; Tang, C.; Liu, X. M.; Wang, C.; Ma, W.; Zhang, Q. Highly selective electrochemical reduction of dinitrogen to ammonia at ambient temperature and pressure over iron oxide catalysts. *Chem. Eur. J.* **2018**, 24, 18494–18501.

(14) Tao, H.; Choi, C.; Ding, L. X.; Jiang, Z.; Hang, Z.; Jia, M.; Fan, Q.; Gao, Y.; Wang, H.; Robertson, A. W.; Hong, S.; Jung, Y.; Liu, S.; Sun, Z. Nitrogen fixation by Ru single-atom electrocatalytic reduction. *Chem.* **2019**, 5, 204–214.

(15) Nazemi, M.; Panikkanvalappil, S. R.; El-Sayed, M. A. Enhancing the rate of electrochemical nitrogen reduction reaction for ammonia synthesis under ambient conditions using hollow gold nanocages. *Nano Energy* **2018**, 49, 316–323.

(16) Sun, Z.; Huo, R.; Choi, C.; Hong, S.; Wu, T. S.; Qiu, J.; Yan, C.; Han, Z.; Liu, Y.; Soo, Y. L.; Jung, Y. Oxygen vacancy enables electrochemical N_2 fixation over WO_3 with tailored structure. *Nano Energy* **2019**, 62, 869–875.

(17) Song, Y.; Johnson, D.; Peng, R.; Hensley, D. K.; Bonnesen, P. V.; Liang, L.; Huang, J.; Yang, F.; Zhang, F.; Qiao, R.; Baddorf, A. P.; Tschaplinski, T. J.; Engle, N. L.; Hatzell, M. C.; Wu, Z.; Cullen, D. A.; Meyer, H. M. III; Sumpter, B. G.; Rondinone, A. J. A physical catalyst for the electrolysis of nitrogen to ammonia. *Sci. Adv.* **2018**, 4, e1700336–8.

(18) Hao, Y. C.; Guo, Y.; Chen, L. W.; Shu, M.; Wang, X. Y.; Bu, T. A.; Gao, W. Y.; Zhang, N.; Su, X.; Feng, X.; Zhou, J. W.; Wang, B.; Hu, C. W.; Yin, A. X.; Si, R.; Zhang, Y. W.; Yan, C. H. Promoting nitrogen electroreduction to ammonia with bismuth nanocrystals and potassium cations in water. *Nat. Catal.* **2019**, 2, 448–456.

(19) Wang, J.; Yu, L.; Hu, L.; Chen, G.; Xin, H.; Feng, X. Ambient ammonia synthesis via palladium-catalyzed electrohydrogenation of dinitrogen at low overpotential. *Nat. Commun.* **2018**, 9, 1795–7.

(20) Pan, J.; Wang, Y.; Zheng, R.; Wang, M.; Wan, Z.; Jia, C.; Weng, X.; Xie, J.; Deng, L. Directly grown high-performance WO_3 films by a novel one-step hydrothermal method with significantly improved stability for electrochromic applications. *J. Mater. Chem. A* **2019**, 7, 13956–13967.

(21) Tian, H.; Cui, X.; Zeng, L.; Su, L.; Song, Y.; Shi, J. Oxygen vacancy-assisted hydrogen evolution reaction of the Pt/WO_3 electrocatalyst. *J. Mater. Chem. A* **2019**, 7, 6285–6293.

(22) Diao, J.; Yuan, W.; Qiu, Y.; Cheng, L.; Guo, X. A hierarchical oxygen vacancy-rich WO_3 with nanowire-array-on-nanosheet-array structure for highly efficient oxygen evolution reaction. *J. Mater. Chem. A* **2019**, 7, 6730–6739.

(23) Kong, W.; Zhang, R.; Zhang, X.; Ji, L.; Yu, G.; Wang, T.; Luo, Y.; Shi, X.; Xu, Y.; Sun, X. WO_3 nanosheets rich in oxygen vacancies for enhanced electrocatalytic N_2 reduction to NH_3. *Nanoscale* **2019**, 11, 19274–19277.

(24) Zhang, L.; Ji, X.; Ren, X.; Ma, Y.; Shi, X.; Tian, Z.; Asiri, A. M.; Chen, L.; Tang, B.; Sun, X. Electrochemical ammonia synthesis via nitrogen reduction reaction on a MoS_2 catalyst: theoretical and experimental studies. *Adv. Mater.* **2018**, 30, 201800191–6.